Angewandte Chemie
Eine Zeitschrift der Gesellschaft Deutscher Chemiker

Supporting Information

N-Heterocyclic Olefins on a Silicon Surface

M. Das, C. Hogan, R. Zielinski, M. Kubicki, M. Koy, C. Kosbab, S. Brozzesi, A. Das, M. T. Nehring, V. Balfanz, J. Brühne, M. Dähne, M. Franz, N. Esser*, F. Glorius**

Supporting Information

Contents

1. Experimental Methods

For scanning tunneling microscopy (STM) and X-ray photoelectron spectroscopy (XPS) experiments, two separate ultra-high vacuum (UHV) chamber systems hosting comparable sample preparation facilities were employed. All experiments were performed at room temperature.

1.1. STM Experiments

STM experiments were performed *in situ* using a home-built STM setup and a commercial control electronics (Nanonis). All images were aquired in constant-current mode using electro-chemically etched W tips, which were cleaned *in-situ* by electron bombardment prior to usage. All STM data was measured at room temperature at a base pressure of 5×10^{-9} Pa.

1.2. XPS Experiments

For XPS measurements of the C 1*s*, B 1*s*, Si 2*p* and N 1*s* core levels, a separate UHV system (base pressure 3×10^{-8} Pa) was used hosting a hemispherical energy analyzer (SPECS Phoibos 100) using monochromatized Al Kα X-rays with $h\nu = 1486.7$ eV (SPECS FOCUS 500 Ellipsoidal Crystal Monochromator and X-Ray source SPECS XR50 M) yielding an instrumental resolution of ∼0.5 eV. The binding energy scale was calibrated to the Au 4*f* line at 84.0 eV using a Au foil in direct contact with the sample holder.

The work function changes were determined by measuring the secondary electron onsets using XPS for the clean Si(111)-B surfaces as well as for the IMe-NHO and IPr-NHO monolayers as described e.g. in Ref. 1. To ensure that all secondary electrons reach the analyzer, a bias of −9 V was applied to the sample.

The core-level spectra were fitted using Voigt line profiles for considering both lifetime and instrumental broadening. Both a constant and a Shirley-type background were used. Tougaard-type backgrounds were also tested only negligibly changing the fit results.

All core-level spectra were measured under an angle of 70° with respect to the surface normal, while the work function measurements were performed in normal emission.

1.3. Sample Preparation

1.3.1. Si(111)-B substrate preparation

The samples were cut from highly B doped Si(111) wafers (Crystec GmbH Berlin, Germany; $\rho < 0.002$ Ωcm and Sil'tronix Silicon Technologies, Archamps, France; 0.0008 Ωcm $< \rho <$ 0.0012 Ωcm). After transferring into the ultra-high vacuum chamber systems, the samples were cleaned by several annealing procedures using direct current heating. The temperature was measured with an infrared pyrometer with an accuracy of ±20 °C. First, the samples were degassed at 600 °C for several hours followed by repeated flash annealing to 1200 °C to remove surface contamination.

Then, the actual Si(111)-B substrate was prepared by annealing the flash-cleaned samples at 950 °C for 30-60 min leading to B surface segregation. In Figure S1, a representative STM image of the obtained Si(111)-B substrate is presented to demonstrate the successful preparation of the $\sqrt{3} \times \sqrt{3}$ reconstruction with low defect density. Additionally, overview XPS spectra were measured for all samples (see Fig. below), showing no remainings of the oxide layer.

1.3.2. NHO deposition

The NHO-molecules were deposited using an analogous method as introduced for NHCs in previous studies.[2,3] The principle is shown in the figure below. We used NHO · CO_2 adducts as precursors for the investigated NHOs IPr-NHO and IMe-NHO (Their synthesis is described in detail in Sec. 3). When heated under UHV conditions, the CO_2 is detached resulting in a molecular beam of free NHO molecules. Home-built evaporators with pyrolytic boron nitride crucibles and crucible temperatures in the range from room temperature to 30 °C were used for evaporation. This results in deposition times between a few seconds and several minutes for the investigated low and high coverage samples, respectively. During NHOs deposition, the sample was held at room temperature and during the whole sample preparation, the pressure did not exceed 2×10^{-7} Pa. During deposition, we monitor the partial pressures for all relevant masses using a quadrupole mass spectrometer installed in the deposition chamber. An example for IMe-NHO is shown below. When heating the evaporator, a strong increase in the CO_2 signal (mass 44) is observed, while the other masses stay almost constant. Only slight increases for masses 16 and 28 are observed additionally, and are assigned to a decomposition of CO_2 into CO (mass 28) and O (mass 16) in the ion source of the mass spectrometer. This data proves that the CO_2 is cleaved off during evaporation and the pure molecules are evaporated. The deposition of clean NHO molecules without any residuals from the NHO · CO_2 adducts is additionally proven by the absence of an O 1*s* signal in the XPS overview spectra presented below.

For NHCs, a degradation of the CO_2 adducts into their associated bicarbonate salts upon exposure to air has been reported. However, for the deposition on the surface it does not seem to matter as the CO_2 adducts as well as the bicarbonate salts both decompose into pure NHCs upon vacuum annealing.[4–7] The NHO · CO_2 adducts were stored under Ar atmosphere in a freezer at −18 °C. Our QMS data (see below) indicates that no degradation of the CO_2 adducts into the bicarbonate salts occurs, as otherwise an increase in the H_2O signal (mass 18) should occur in addition to CO_2 what is not observed. Thus, we conclude that the NHO · CO_2 adducts remained stable during storage and the evaporation occurs via loss of the CO_2 molecule as shown in A in the following figure.

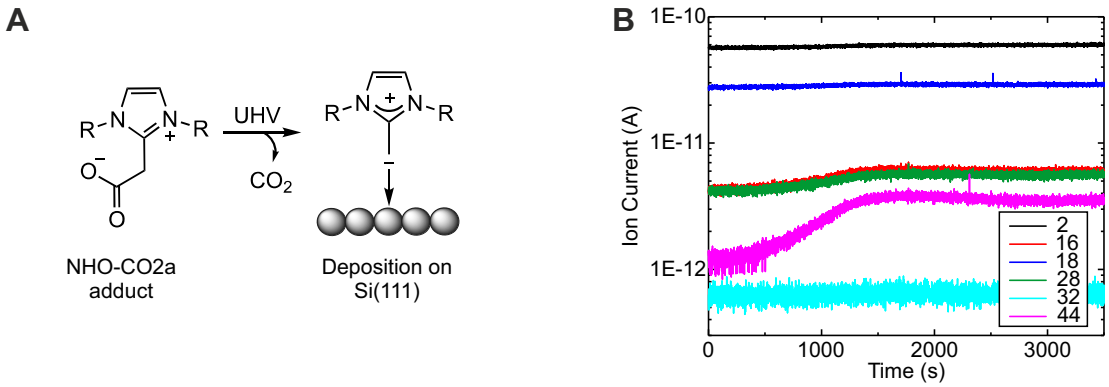

(A) Principle of the NHO deposition. (B) Quadrupole mass spectroscopy data measured during IMe-NHO evaporation.

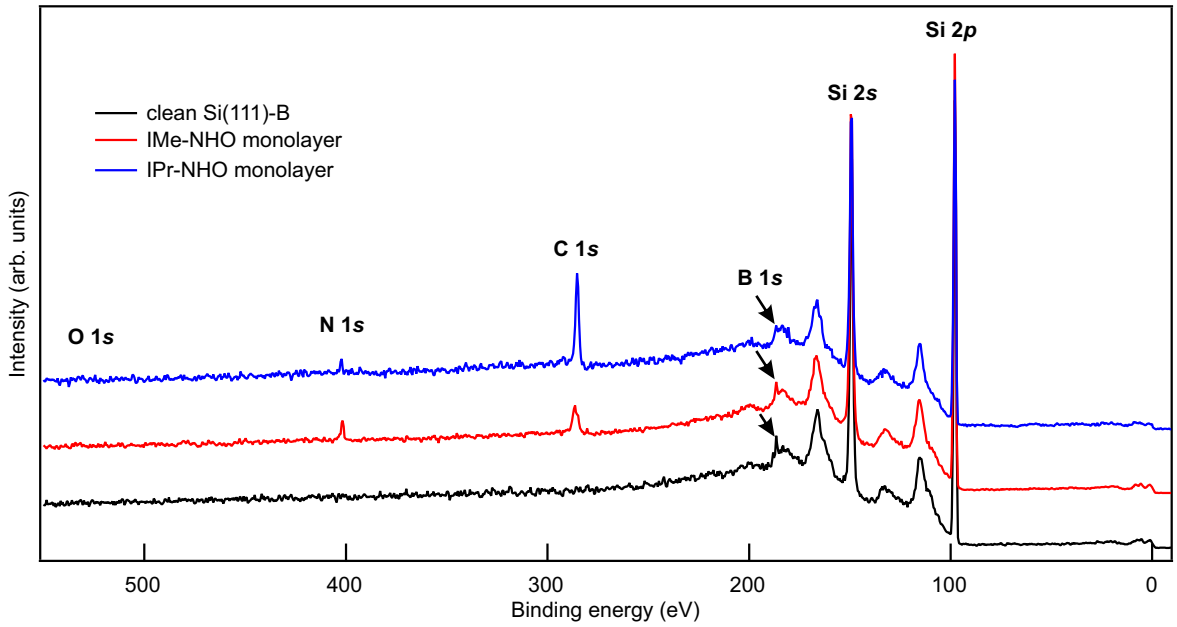

XPS overview spectra for a clean Si(111)-B sample and samples covered with IMe-NHO and IPr-NHO monolayers. The B 1s signals (indicated by arrows) are located on a plasmon loss satellite peak of the Si 2s core level.

2. Computational Details

Density functional theory (DFT) calculations were performed using the quantum-ESPRESSO code [8] within a planewave (cutoff 50 Ry) and norm-conserving pseudopotential framework. The Perdew-Burke-Ernzerhof (PBE) exchange-correlation functional was used along with the semi-empirical Grimme-D3 van der Waals (vdW) correction including Becke-Johnson damping. [9] The Si(111)-B surface was modelled using periodic supercells containing slabs four Si-bilayers thick, back-terminated by H, and separated by 25 Å of vacuum. Dipole corrections in the vacuum were used throughout. To account for different molecular coverages, surface unit cells ranging from $2\sqrt{3}\times 2\sqrt{3}$ to $4\sqrt{3}\times 4\sqrt{3}$ were adopted, with corresponding **k**-point meshes ranging from $4\times 4\times 1$ to Γ-point only. Relaxed geometries are shown in Fig. S4. Geometry optimizations were carried out using very tight thresholds of 2.6 meV/Å on the atomic forces. All DFT simulations were performed assuming a static crystal, i.e. at zero temperature. For the calculation of rotational barriers (Fig. S2) the nudged elastic band method [10] using climbing images (CI-NEB) was used. A 3×3 cell (Γ-point only), and a thinner 3-bilayer slab (1 bilayer fixed) was used for CI-NEB runs. STM images and profiles were modelled using the Tersoff-Hamann approximation [11] using the same sample voltages as in the respective experimental images. Work functions were computed as the difference between the electrostatic potential in the vacuum and the slab Fermi level. [12] Voronoi deformation density (VDD) charges [13] were computed in $3\sqrt{3}\times 3\sqrt{3}$ cells using the `critic2` code. [14] A dense grid of $600\times 600\times 1200$ yielded VDD charges converged to about 2–3 millielectrons. Images of geometries, ELF, and STM were prepared with VESTA. [15]

3. Synthesis

3.1. Synthesis of starting materials

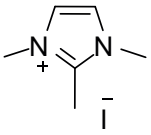

1,2,3-Trimethyl imidazolium iodide (IMe-NHO · HI): The title compound was synthesized by following the literature known method.[16] Commercially available 1,2-dimethylimidazole (3.8 g, 40.0 mmol, 1.0 equiv.) was taken in a Schlenk flask, then 20 mL acetonitrile and methyl iodide (3.7 mL, 60.0 mmol, 1.5 equiv.) were added to the flask. The mixture was stirred heated at 40 °C for 2 h. After cooling the flask to room temperature, solvent was evaporated under reduced pressure. The residue was washed with large amount of THF and hexane, after drying overnight under vacuum the product was isolated as a white solid (8.5 g, 35.7 mmol, 89% yield).

^{1}H NMR (400 MHz, DMSO-d_6): δ (ppm) 7.60 (s, 2H), 3.76 (s, 6H), 2.56 (s, 3H).
^{13}C NMR (101 MHz, DMSO-d_6): δ (ppm) 144.7, 121.9, 34.8, 9.4.
HRMS (ESI): m/z calculated for $C_6H_{11}N_2$ $[M–I]^+$ 111.0916; found 111.0914.

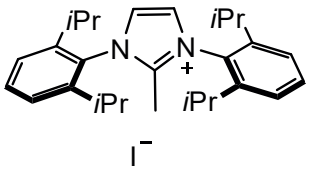

1,3-Bis(2,6-diisopropylphenyl)-2-methyl-1*H*-imidazol-3-ium iodide
(IPr-NHO · HI): The title compound was synthesized by following a modified literature known method.[17] To a white suspension of 1,3-bis(2,6-diisopropylphenyl)-1*H*-imidazol-3-ium chloride (850 mg, 2.0 mmol, 1.0 equiv.) in 10 mL of THF at -78 °C was added dropwise *n*BuLi (1.4 mL, 1.6 M in hexane, 1.1 equiv.). The reaction was stirred for 10 min at -78 °C and then the resulting clear solution was warmed to room temperature and stirred for another 5 min. Methyl iodide (137 µL, 2.2 mmol, 1.1 equiv.) was added at -78 °C to the reaction mixture which results a white precipitate. After the addition, the stirring was continued for another 10 min at -78 °C and then warmed to room temperature. The precipitate was filtered and washed with hexane, after drying for overnight in vacuum the product was collected as a white solid (781 mg, 1.47 mmol, 74% yield).

^{1}H NMR (400 MHz, CD_2Cl_2): δ (ppm) 7.99 (s, 2H), 7.72 – 7.63 (m, 2H), 7.51 – 7.41 (m, 4H), 2.37 – 2.23 (m, 4H), 2.13 (s, 3H), 1.36 – 1.18 (m, 24H).
^{13}C NMR (101 MHz, CD_2Cl_2): δ (ppm) 146.3, 145.3, 133.1, 129.2, 125.9, 29.6, 24.8, 23.5, 11.2.
HRMS (ESI): m/z calculated for $C_{28}H_{39}N_2$ $[M–I]^+$ 403.3107, found 403.3106.

3.2. General procedure for Synthesis of NHO · CO_2 adducts

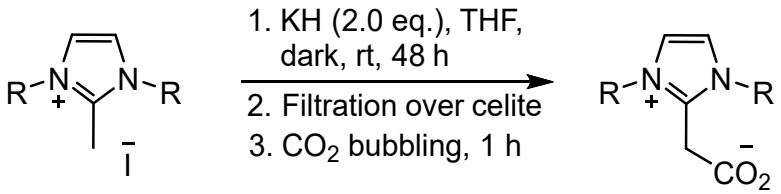

R = Me, Dipp

IMe-NHO · CO_2, when R = Me
IPr-NHO · CO_2, when R = Dipp

We followed a modified procedure reported by Lu and coworkers for synthesizing the CO_2 adduct for NHO molecules.[16] 2-methylated imidazolium salt (1.0 equiv.) was taken in an oven dried Schlenk flask and KH (2.0 equiv.) was added to the flask from glovebox. Dry THF (0.2 M) was added under argon and the flask was covered with aluminum foil to protect the reaction mixture from light. The reaction was stirred for 2 days at room temperature in dark. After that, the suspension

was filtered under argon through Celite® pad into a flame dried Schlenk flask. Carbon di-oxide dried with conc. Sulfuric acid was bubbled through the filtrate for 30 min. A white precipitate was formed during the time, it was collected by filtration under air and washed with large amount of dry hexane and diethyl ether. Overnight drying in high vacuum gave us the product as a white powder. The product was stored inside the fridge after flushing the vial with argon.

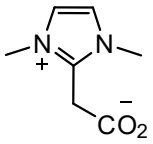

2-(1,3-dimethyl-1H-imidazol-3-ium-2-yl)acetate (IMe-NHO · CO_2): The title compound was synthesized according to the general procedure for synthesis of NHO · CO_2 adducts from 1,2,3-trimethyl imidazolium iodide **IMe-NHO · HI** (476.1 mg, 2.0 mmol, 1.0 equiv.) and KH (160.4 mg, 4.0 mmol, 2.0 equiv). The product was obtained as white solid (150 mg, 0.97 mmol, 49% yield).

^{1}**H NMR** (400 MHz, D_2O): δ (ppm) 7.34 (s, 2H), 3.95 (s, 2H), 3.76 (s, 6H).
^{1}3**C NMR** (101 MHz, D_2O): δ (ppm) 171.5, 143.1, 122.2, 34.6, 32.0.
HRMS (ESI): m/z calculated for $C_7H_{11}N_2O_2$ $[M+H]^+$: 155.0815; found: 155.0819, m/z calculated for $C_6H_{11}N_2$ $[(M–CO_2)+H]^+$: 111.0916; found: 111.0919.
ATR-FTIR (cm^{-1}): 3103, 3050, 2939, 1652, 1612, 1542, 1516, 1457, 1440, 1421, 1386, 1342, 1324, 1265, 1195, 1132, 1109, 1096, 1041, 1030, 994, 892, 868, 839, 826, 799.

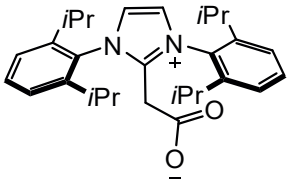

2-(1,3-bis(2,6-diisopropylphenyl)-1H-imidazol-3-ium-2-yl)acetate (IPr-NHO · CO2): The title compound was synthesized according to the general procedure for synthesis of NHO · CO_2 adducts from 1,3-bis(2,6-diisopropylphenyl)-2-methyl-1H-imidazol-3-ium iodide **IPr-NHO · HI** (530.5 mg, 1.0 mmol, 1.0 equiv.) and KH (80.2 mg, 2.0 mmol, 2.0 equiv.). The product was obtained as white solid (230 mg, 0.51 mmol, 52% yield).

^{1}**H NMR** (300 MHz, D_2O): δ (ppm) 7.73 (s, 2H), 7.26 – 7.02 (m, 2H), 6.99 – 6.85 (m, 4H), 1.96 – 1.66 (m, 4H), 1.55 (s, 2H), 0.86 – 0.52 (m, 24H).
^{1}3**C NMR** (101 MHz, D_2O): δ (ppm) 145.4, 132.2, 129.2, 125.1, 124.6, 28.8, 23.6, 22.2.
HRMS (ESI): m/z calculated for $C_{29}H_{39}N_2O_2$ $[M+H]^+$: 447.3006; found: 447.2985, m/z calculated for $C_{28}H_{39}N_2$ $[(M–CO_2)+H]^+$: 403.3107; found: 403.3089.
ATR-FTIR (cm^{-1}): 2961, 2870, 1674, 1653, 1641, 1634, 1613, 1607, 1559, 1506, 1501, 1456, 1306, 1060, 809, 767.

During the synthesis of the NHO · CO_2 adducts, we have purified all the corresponding intermediates separately and characterized them by NMR and HRMS. Therefore, from all analytical data, it can be concluded that the final compounds (IMe-NHO · CO_2 and IPr-NHO · CO_2 adducts) were pure enough which was additionally proved by pushrod mass-spectrometry data. All analytical data is presented below. Furthermore, we use comparable purification methods for NHC · CO_2 adducts and we have not observed any issues with impurities with NHC. Also, evaporation of CO_2 adducts is a really clean process because any remaining salts stay in the crucible.

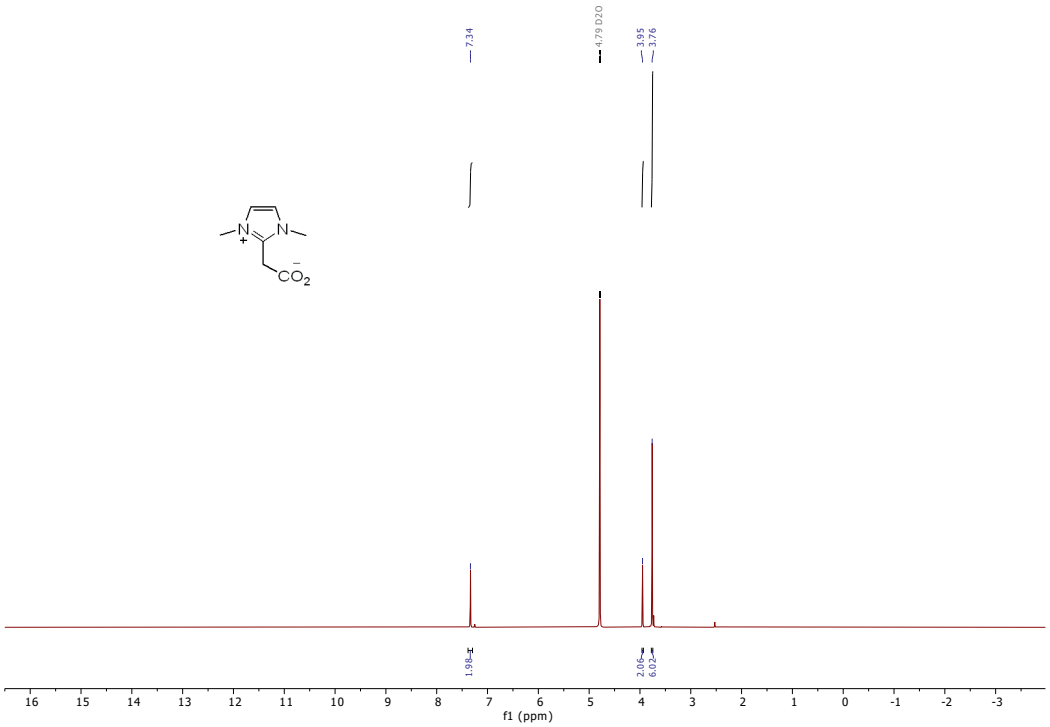
7.34
4.79 D2O
3.95
3.76
1.98
2.06
6.02
f1 (ppm)

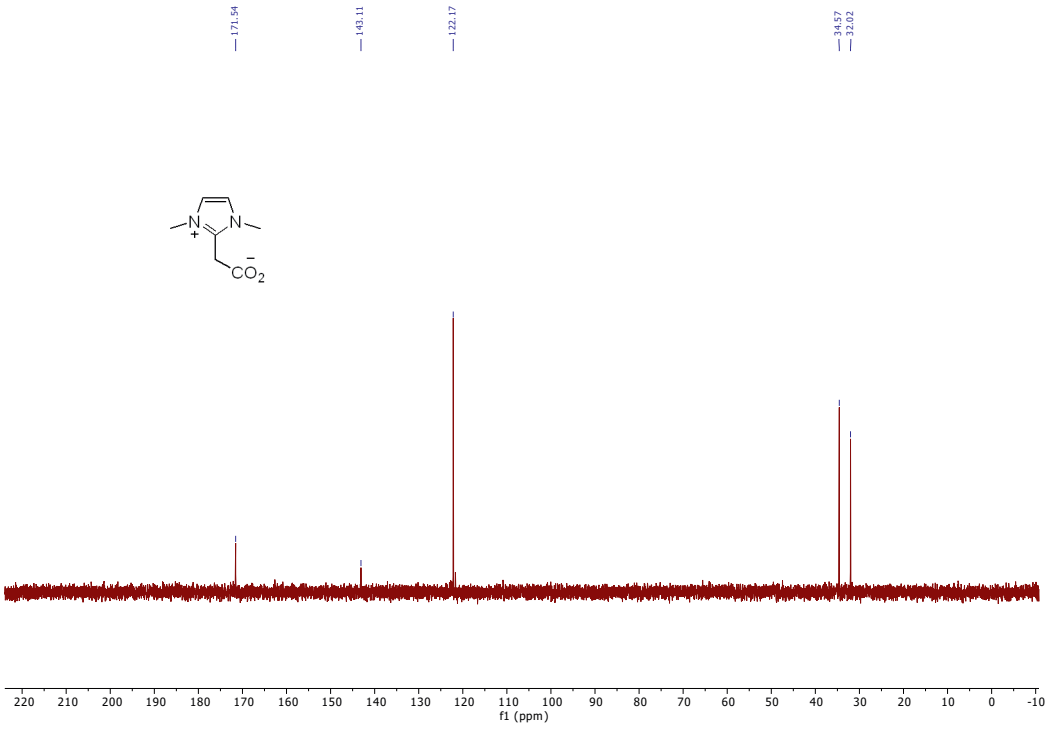
171.54
143.11
122.17
34.57
32.02
f1 (ppm)

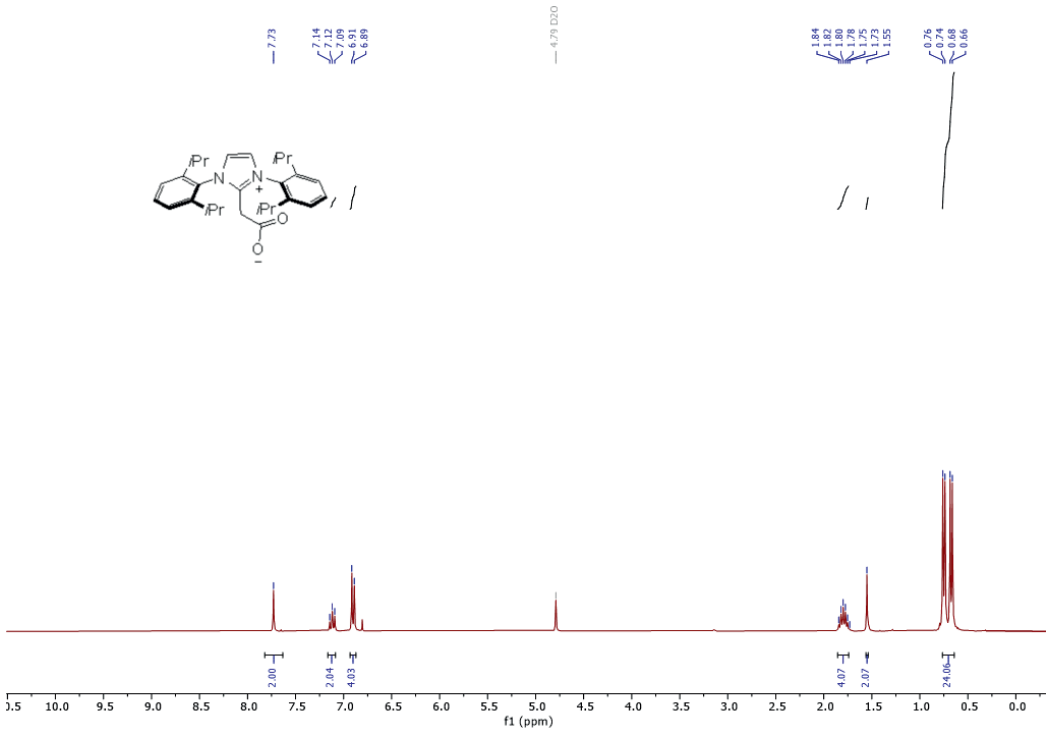
7.73
7.14
7.12
7.09
6.91
6.89
4.79 D2O
1.84
1.82
1.80
1.78
1.75
1.73
1.55
0.76
0.74
0.68
0.66
iPr
iPr
iPr
iPr
O
O
2.00
2.04
4.03
4.07
2.07
24.06
f1 (ppm)

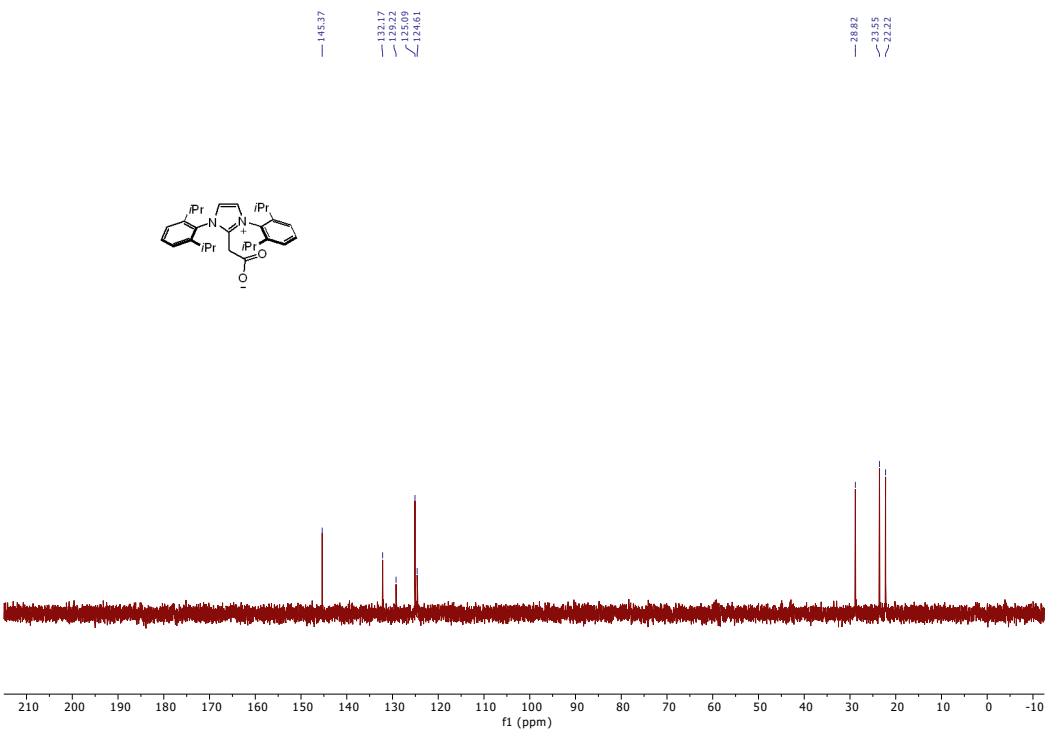
145.37
132.17
129.22
125.09
124.61
28.82
23.55
22.22
iPr
iPr
iPr
iPr
O
O
f1 (ppm)

A IMe-NHO-CO_2

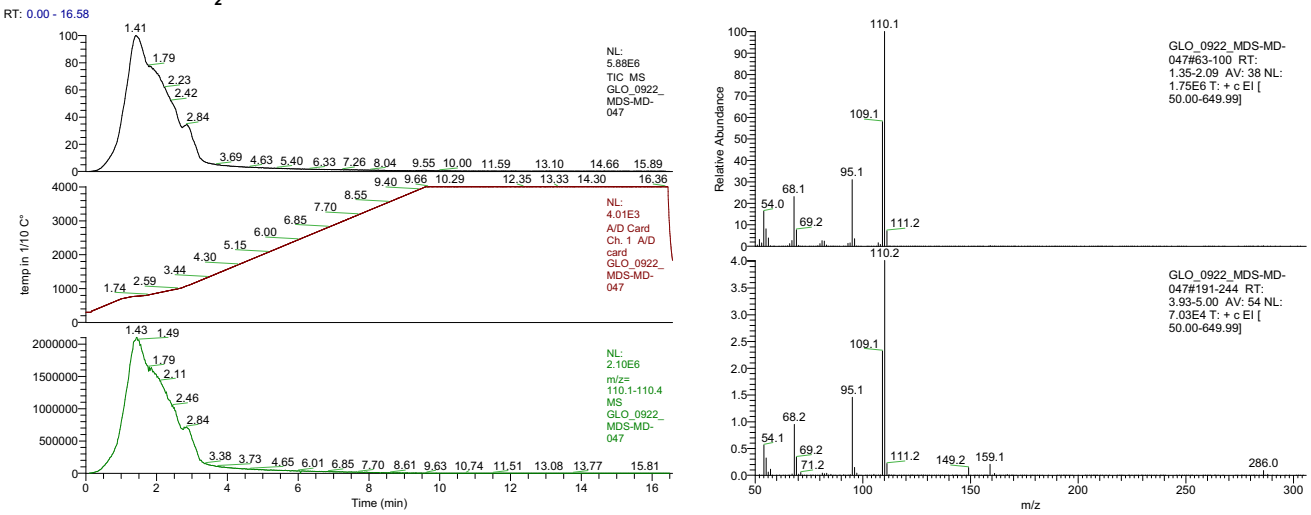

B IPr-NHO-CO_2

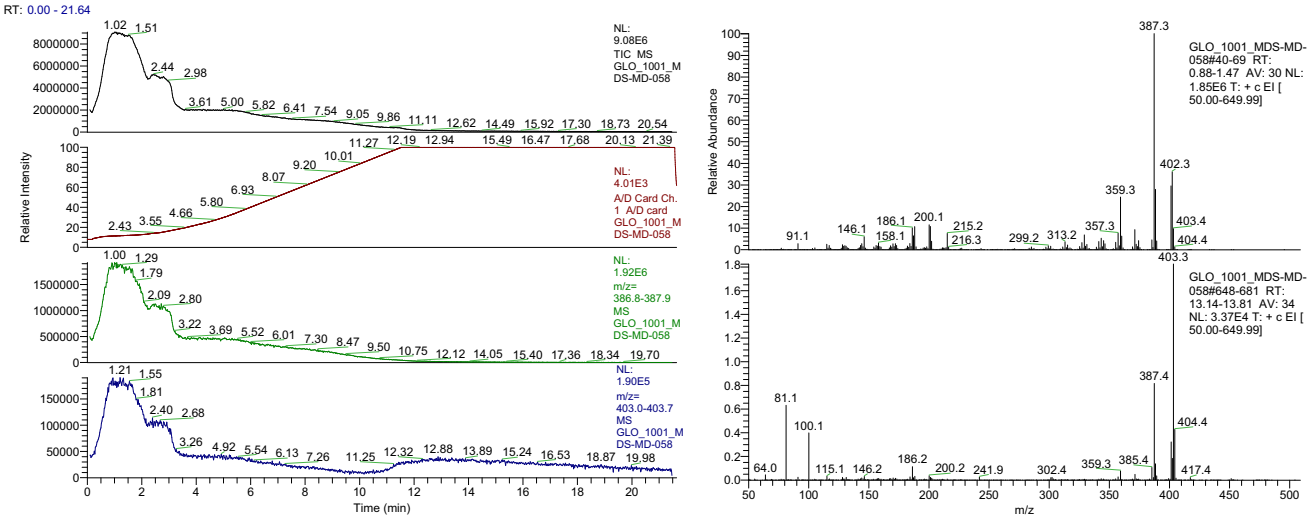

Pushrod MS data for thermally induced decarboxylation of (A) IMe-NHO · CO_2 where the right image shows the mass of free IMe-NHO at 110.1 after decarboxylation, and (B) IPr-NHO · CO_2 adduct where the right image shows the mass of free IPr-NHO at 402.3 after decarboxylation. Additionally, some masses corresponding to molecules fragmented during ionization are observed.

4. Supplementary Figures and Tables

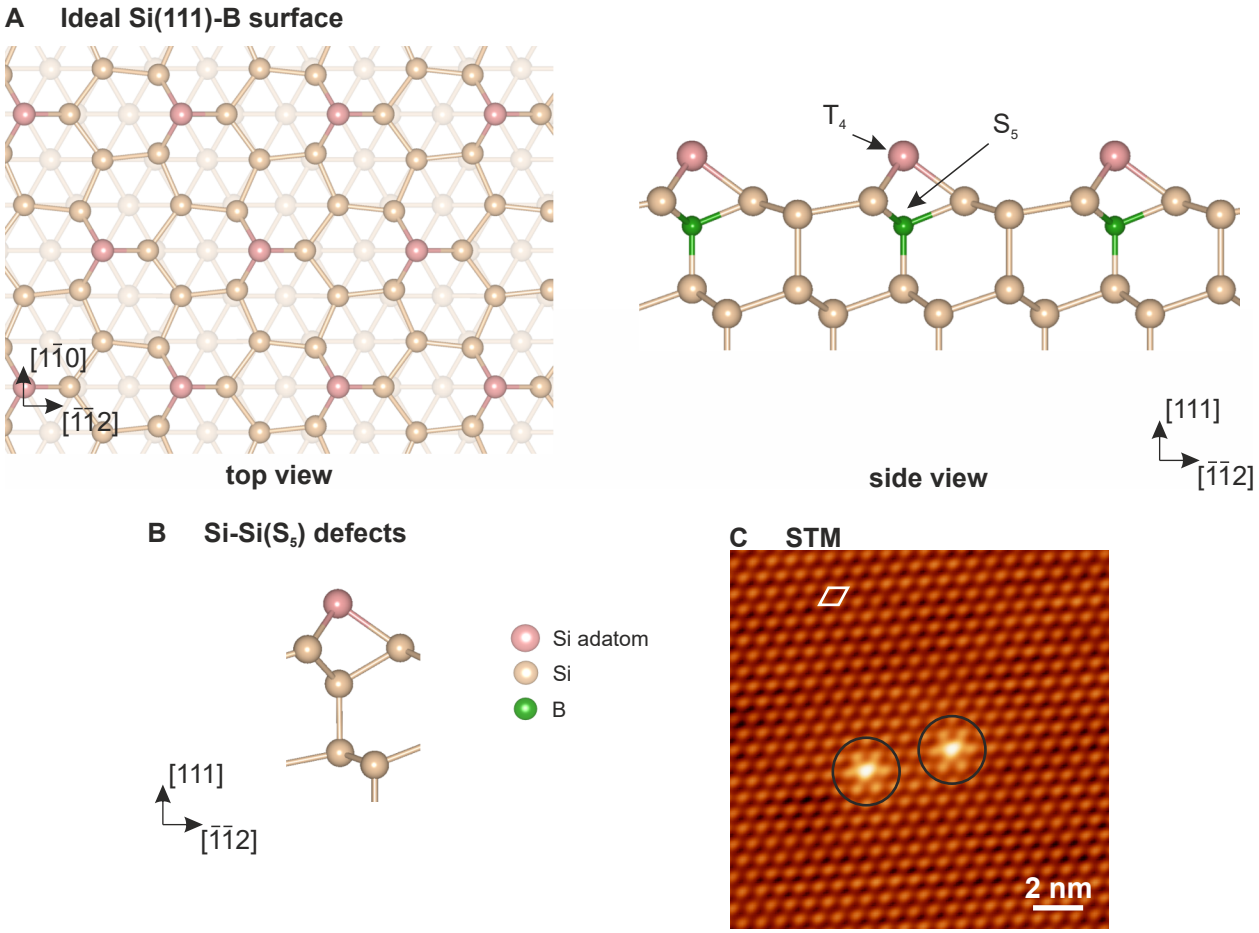

Figure S1. The Si(111)-B surface. (A) Structure model for the $\sqrt{3} \times \sqrt{3}$ reconstruction of the Si(111)-B surface in top view and side view. The B atoms are incorporated on subsurface S_5 lattice sites, while Si adatoms form on top of the B atoms on T_4 lattice sites.[18,19] For a more detailed description of these lattice sites see e.g. Ref. 20. (B) Structure model for the Si-Si(S_5) defect, which is a commonly appearing point defect. Here, the Si atom underneath the adatom is not substituted by a B atom leading to an unpassivated site. (C) STM image of the surface (sample voltage $V_T = +1.3$ V; tunneling current $I_T = 130$ pA). A $\sqrt{3} \times \sqrt{3}$ unit cell is indicated in white. In addition, two Si-Si(S_5) defects are present in the image as indicated by the black circles.

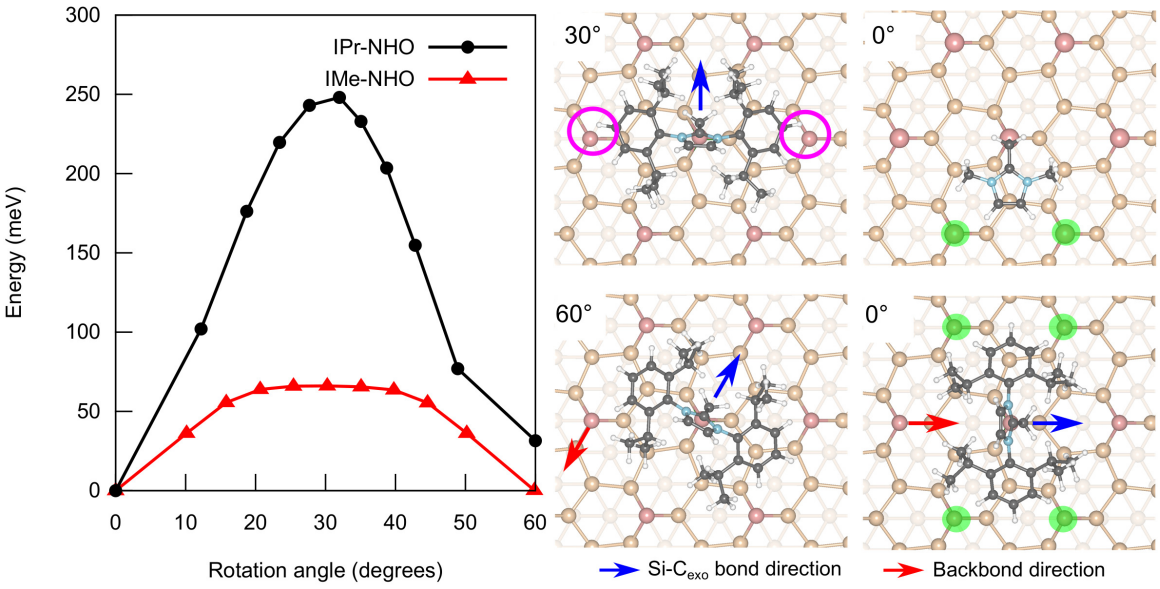

Figure S2. (A) Calculated rotation barriers for isolated IMe-NHO (red line, triangles) and IPr-NHO molecules (black line, circles) on the Si(111)-B surface, using the nudged elastic band method. Minimum energy orientations occur when wingtips (IPr-NHO) or backbone (IMe-NHO) are aligned between pairs of Si adatoms (shaded green circles). For IPr-NHO, the slight difference between 0° and 60° is due to the opposite relative orientations of the Si adatom backbonds and the Si–C_{exo} bond. Due to the substrate symmetry, this leads to three equivalent (or six almost equivalent) orientations of the molecules on the surface. The maximum energy barrier occurs at $30°, 90°$,... due to steric interactions of the wingtips (IPr-NHO) or the backbone (IMe-NHO) with nearby Si adatoms (magenta circles), with a contribution from strain at the Si–C_{exo} bond. The computed barrier of 220–250 meV should weakly hinder rotation at room temperature (RT). The very low energy barrier of 66 meV in IMe-NHO allows it to rotate almost freely around the C–Si bond at RT, consistent with the round shape observed in the STM images. Since the C–Si backbond is never aligned with the molecular axis at its minimum energy orientation angle, there are six equivalent orientations in this case.

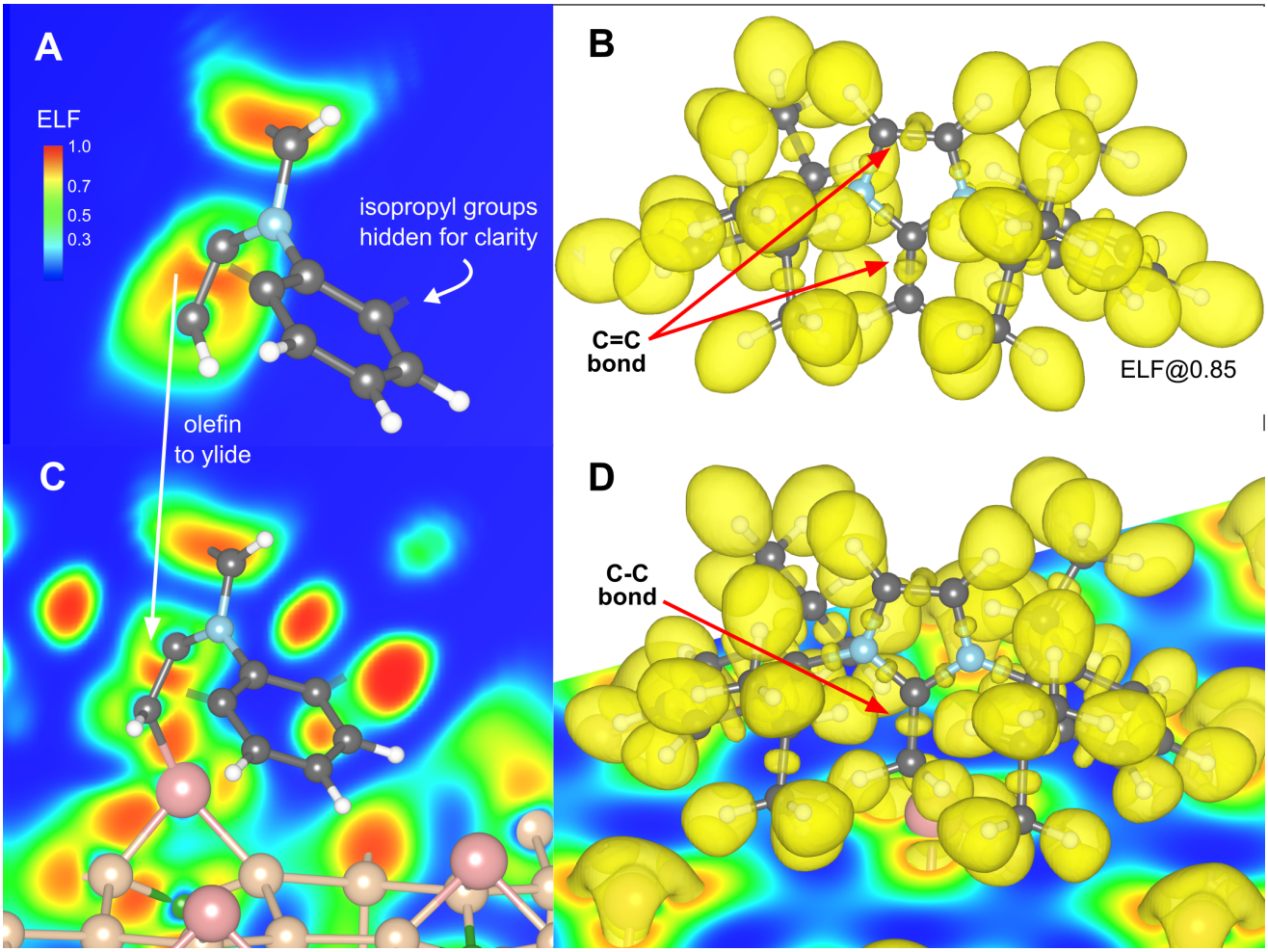

Figure S3. (A) Electron localization function (ELF) for gas phase IPr-NHO. The plane intersects the C_{exo} and C_{endo} atoms and lies perpendicular to the central ring. The four isopropyl groups have been hidden for clarity. (B) ELF isosurface at 0.85, corresponding to high electron density. (C,D) As (A,B) for IPr-NHO adsorbed on Si(111)-B. A horizontal plane intersecting the Si adatoms has been added for clarity in panel (D).

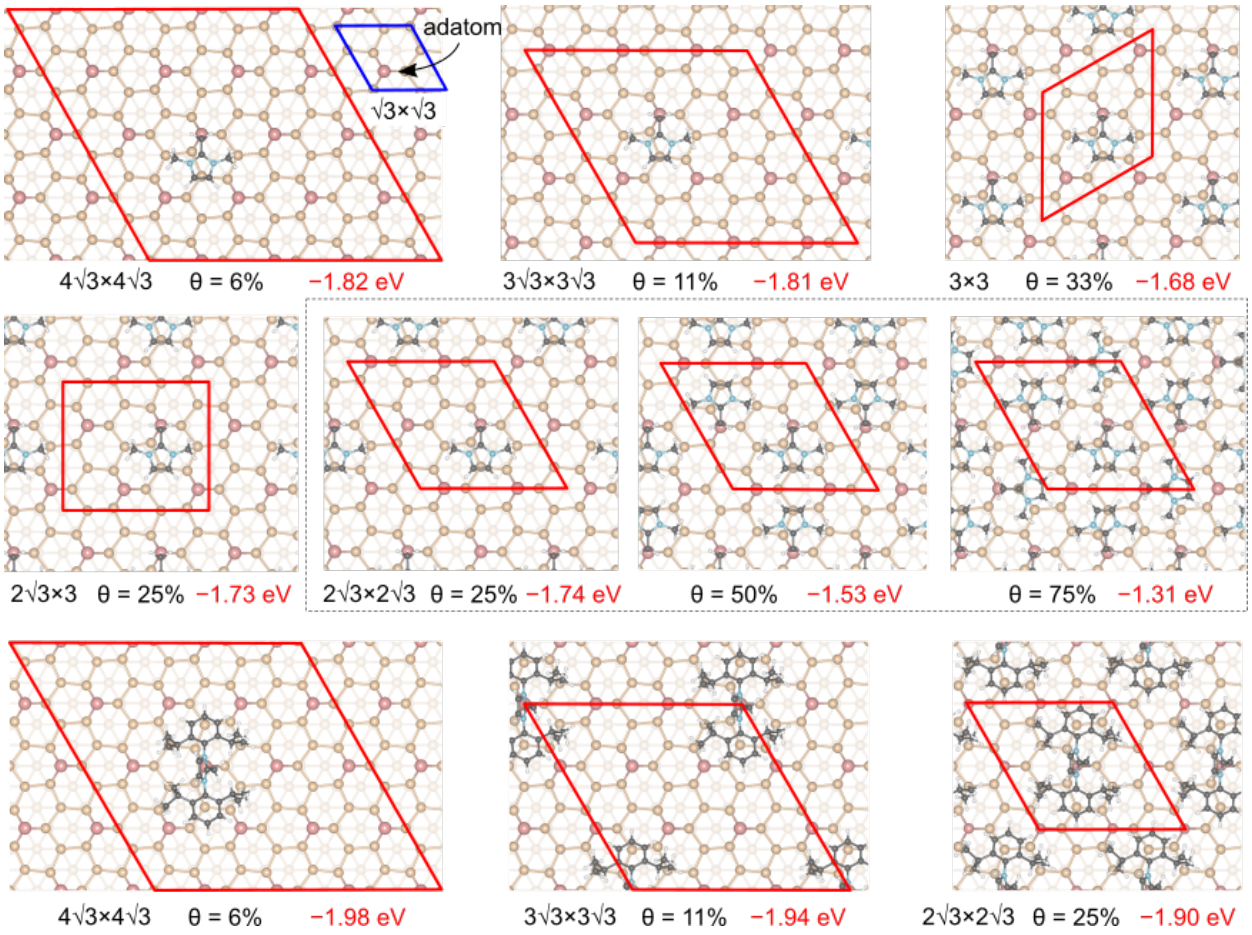

Figure S4. Geometry of IMe-NHO (top rows) and IPr-NHO (bottom row) adsorption on Si(111)-B at different coverages. Coverage θ is reported as a percentage of adatom coverage (i.e. molecules per $\sqrt{3} \times \sqrt{3}$ cell, see blue unit cell indicated). Adsorption energy is reported in eV per molecule. Surface unit cells are shown in red.

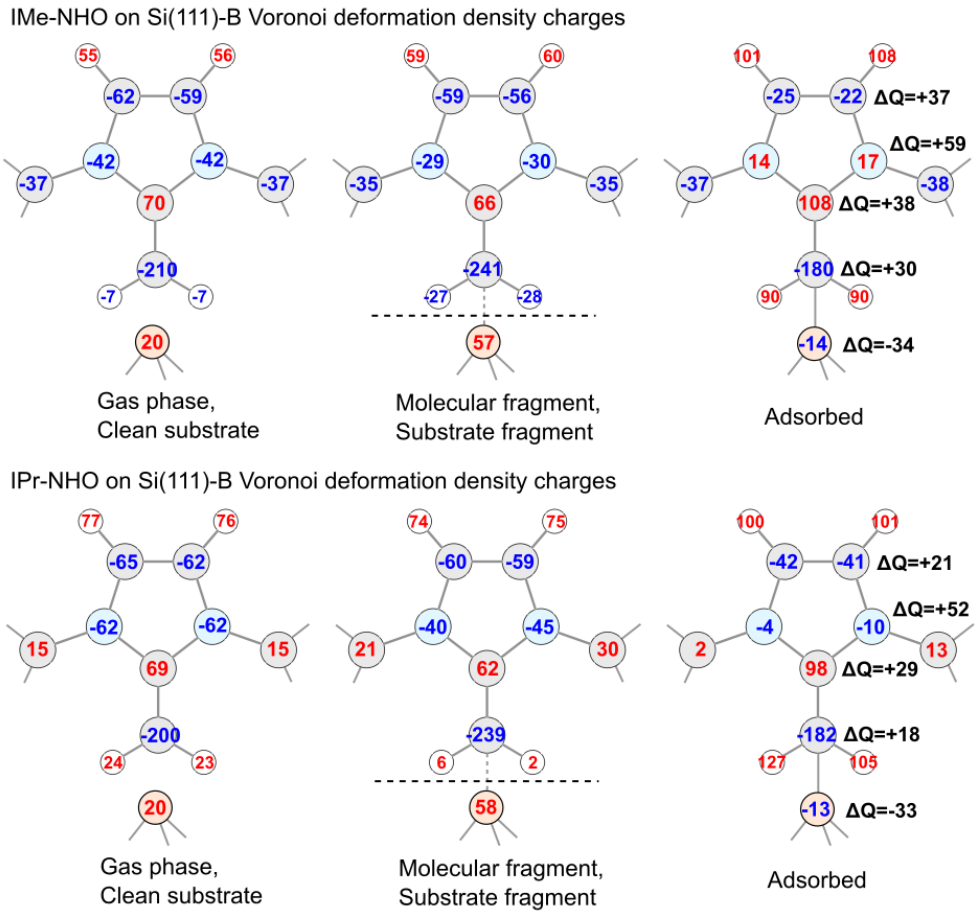

Figure S5. Voronoi deformation density (VDD) atomic charges (Q, in millielectrons) for IMe-NHO and IPr-NHO. VDD charges are reported for (left) the gas phase and adatom of the pristine Si(111)-B substrate, respectively; (right) for the complete adsorbed system, with NHO bonded to the adatom; and (center) for the two fragments of the adsorbed system (i.e. the separated molecule and substrate in their adsorbed geometries). Due to the large geometrical deformation of the NHOs upon adsorption, we report the change (redistribution) ΔQ in atomic charge (for selected atoms) with respect to the gas phase/pristine geometries; note that ΔQ is even larger with respect to the fragment geometries. For clarity only the first C atom in the side groups is shown in all cases. Molecular geometries are schematically shown. Horizontal dashed line indicates the partitioning of the two fragments. Symmetry has not been imposed, hence an integration-grid-induced error of 2–3 millielectrons is evident.

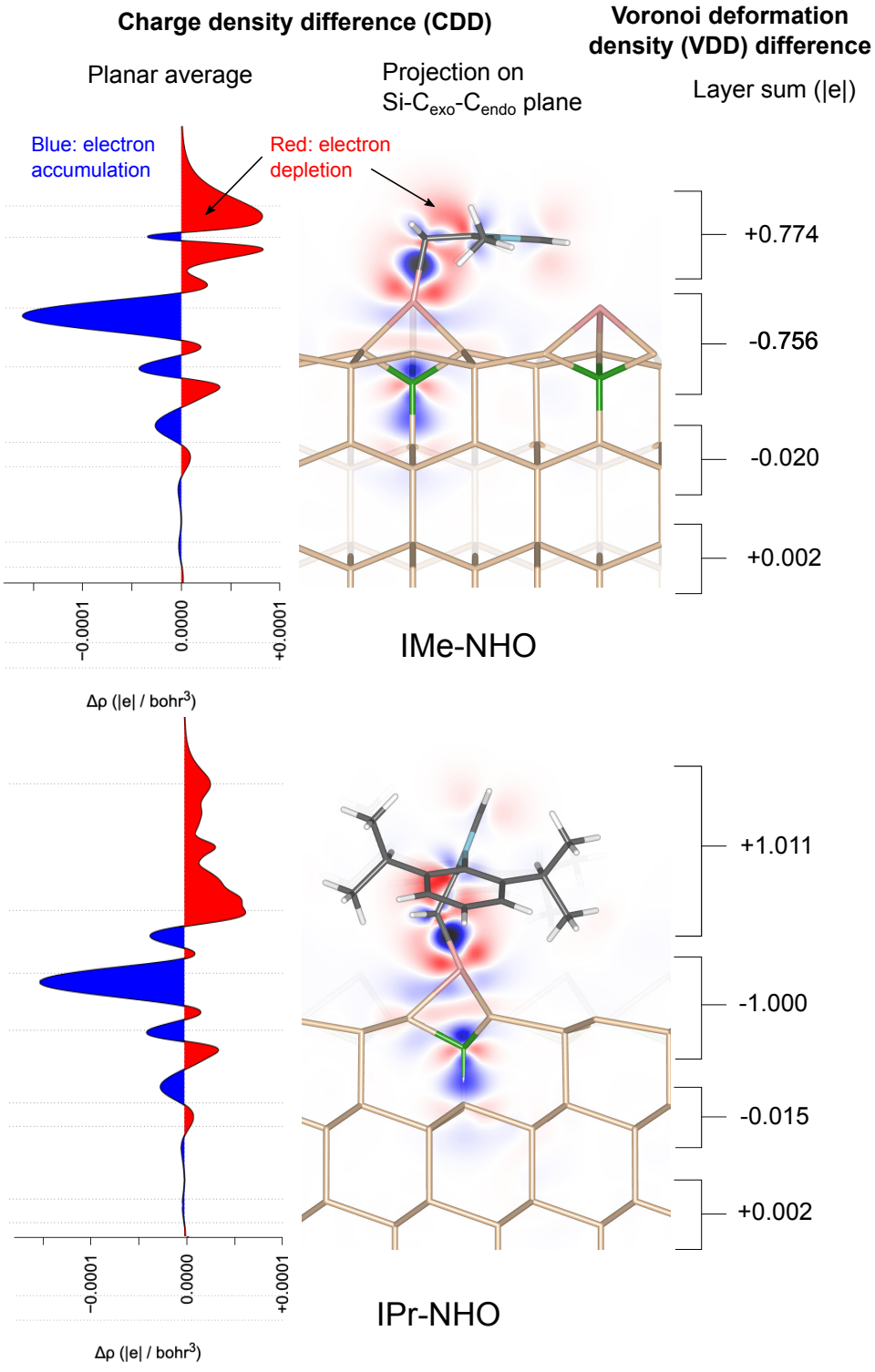

Figure S6. Left: Planar-averaged and plane-projected charge density difference $\Delta\rho = -(\rho_{\mathrm{NHO/surf}} - \rho_{\mathrm{NHO}} - \rho_{\mathrm{surf}})$, for NHO adsorption on Si(111)-B, where the NHO and surface fragments assume their adsorbed geometry. Right: Voronoi deformation density charge differences (ΔQ, in electrons) summed over the atoms in the indicated regions, with respect to the gas phase molecule and pristine surface. Note that CDD and VDD have been defined here to give consistent signs, i.e. positive values indicate electron depletion (shown in red). Dipoles due to charge transfer and charge redistribution both contribute to the work function reduction.

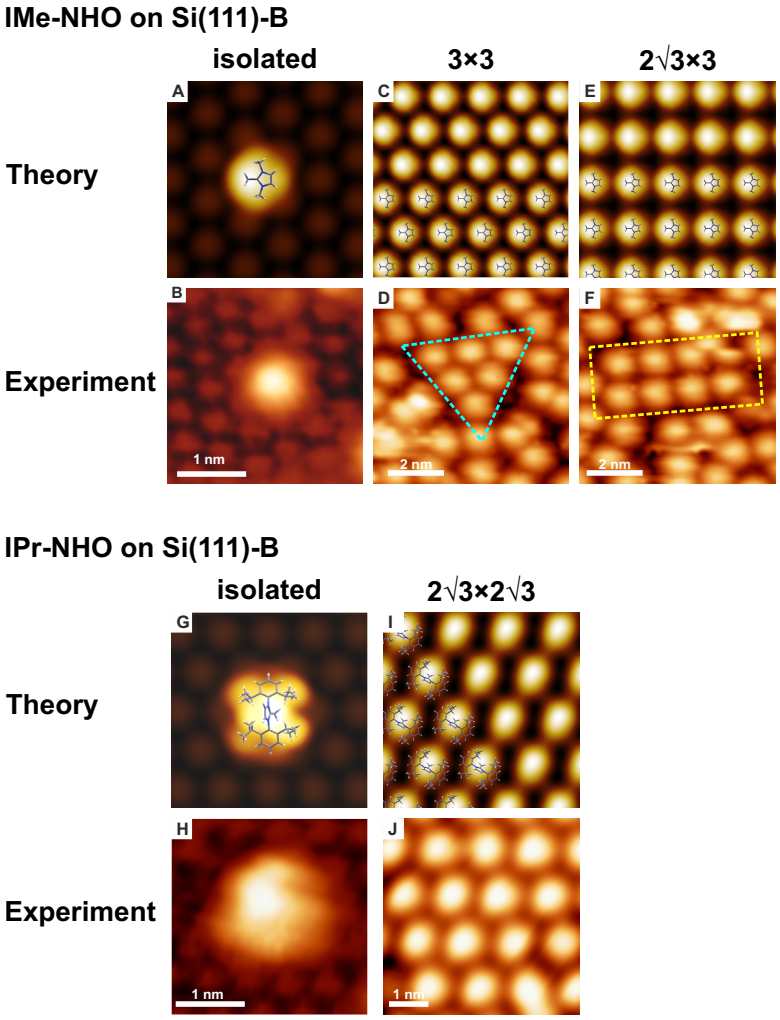

Figure S7. Comparison of simulated and experimental STM images of both investigated NHO molecules on Si(111)-B for the different coverages: (A,B) Isolated IMe-NHO molecule ($V_T = -2.0$ V; $I_T = 10$ pA). (C,D) Ordered domains of the IMe-NHO monolayer with 3×3 periodicity ($V_T = -2.0$ V; $I_T = 10$ pA). (E,F)Ordered domains of the IMe-NHO monolayer with $2\sqrt{3} \times 3$ periodicity ($V_T = -2.0$ V; $I_T = 10$ pA). (G,H) Isolated IPr-NHO molecule ($V_T = -2.8$ V; $I_T = 20$ pA). (I,J) Ordered IPr-NHO monolayer with $2\sqrt{3} \times 2\sqrt{3}$ periodicity ($V_T = +2.8$ V; $I_T = 15$ pA).

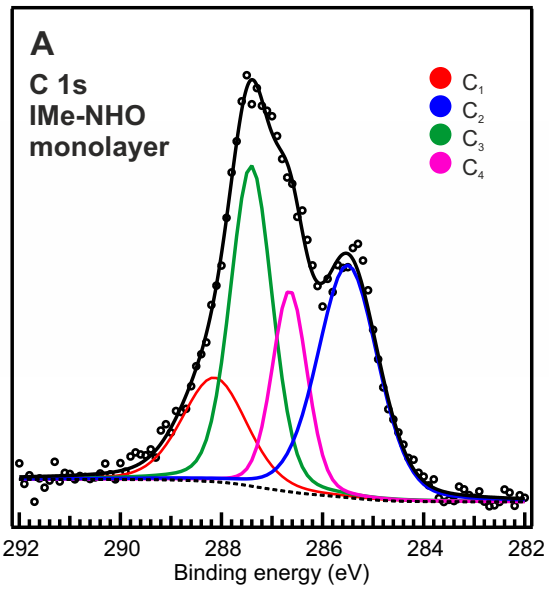

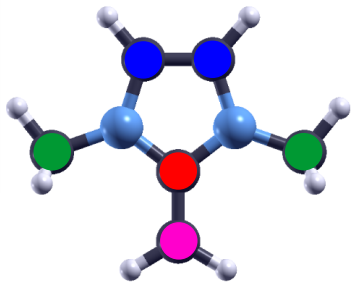

C

Component	CLS IMe-NHC theory (eV)	CLS IMe-NHC experiment (eV)	CLS IMe-NHO experiment (eV)
C_1	-1.12	-1.10	+0.73
C_2	-0.39	-0.39	-1.73
C_3	0	0	0 (287.41)
C_4	-	-	-0.76

Figure S8. (A) C 1*s* core-level spectrum of the IMe-NHO monolayer. (B) Assigment of the components to the different carbon atom sites in the molecule, i.e. the C atoms in the methyl groups (C_3) and the backbone (C_2) as well as $C_{endo}(C_1)$ and $C_{exo}(C_4)$. (C) Comparison of the core-level shifts (CLSs) obtained here for IMe-NHO with those found for IMe-NHC in our previous study using XPS and DFT.[3] The large differences to the spectrum of the corresponding NHC strongly point towards a different adsorption geometry. The larger overall width of the spectrum is related to the larger CLSs assigned to the larger molecule-substrate interaction in the flat-lying geometry as well as to the additional component C_4 from C_{exo}. On the other hand, the larger widths of each component are assigned to a superposition from spectra at different positions due to the rotation of the molecules. In the ylide form, a large positive (negative) charge is present at $C_{endo}(C_{exo})$ leading to a weaker (stronger) screening of the nuclear coulomb potential and the observed higher (lower) binding energies.

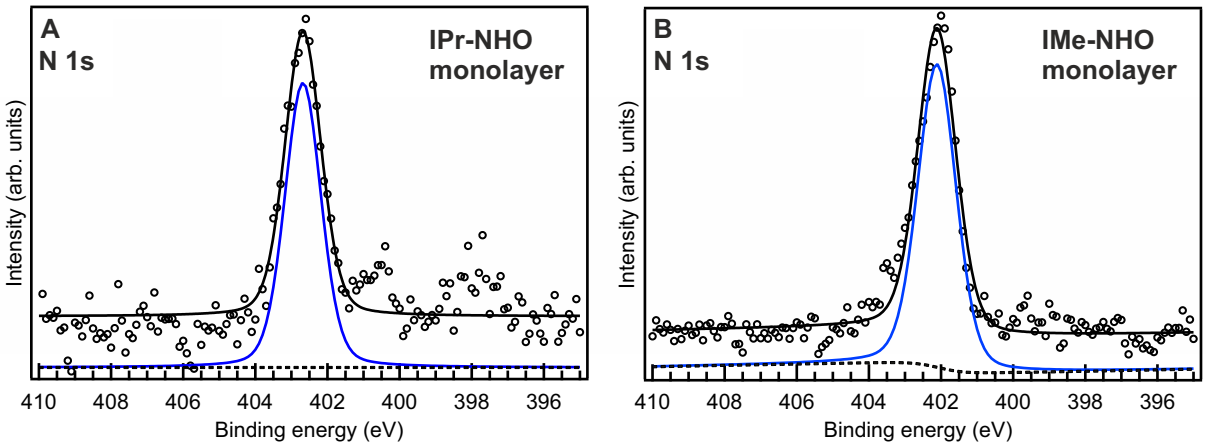

Figure S9. N $1s$ core-level spectra for (A) the IPr-NHO monolayer on Si(111)-B and (B) the IMe-NHO monolayer on Si(111)-B. Both consist of a single component being located at 402.7 eV for IPr-NHO and 402.1 eV for IMe-NHO.

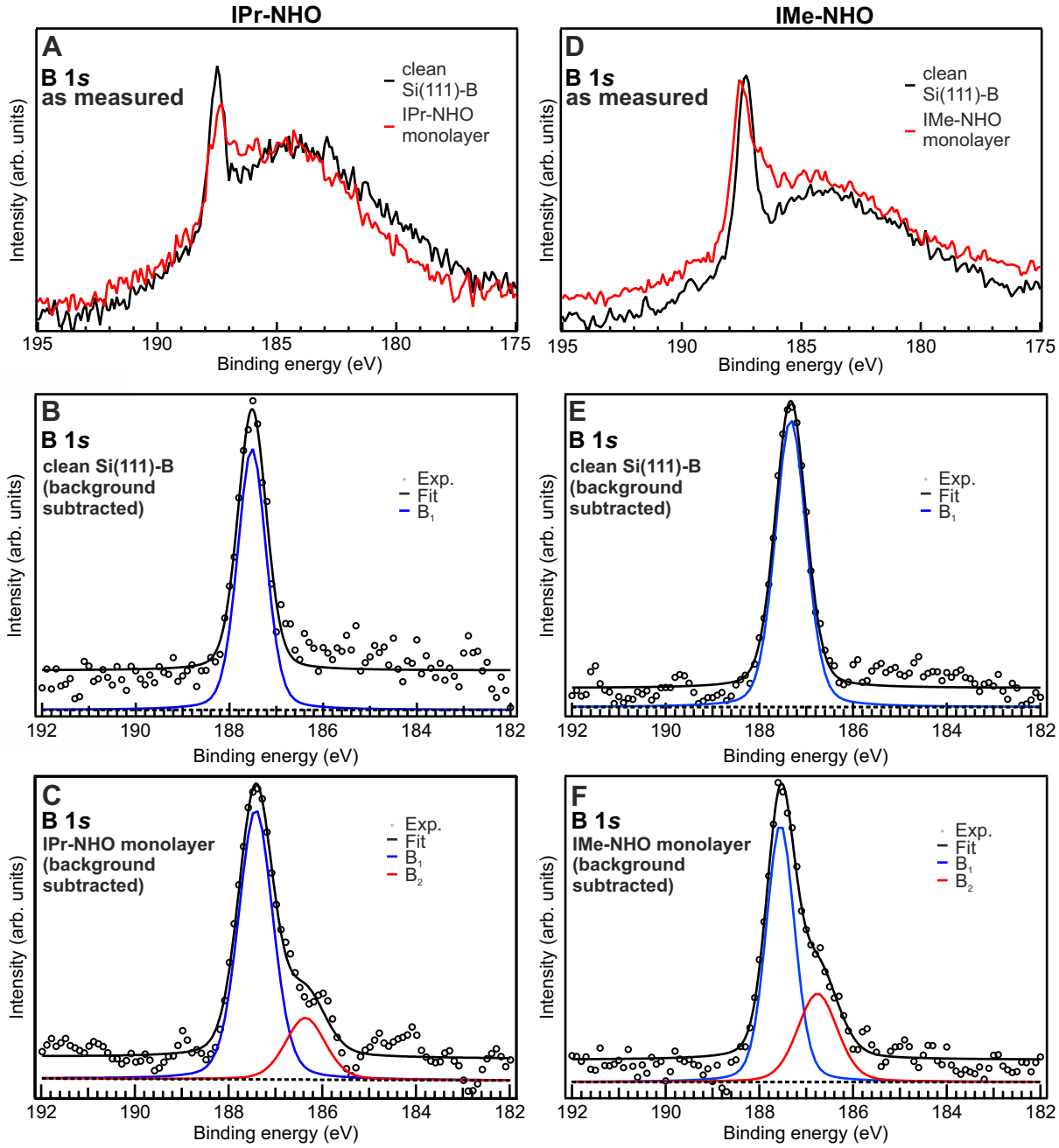

Figure S10. B $1s$ core-level spectra. (A,D) Raw spectra also containing the broad background from a plasmon loss satellite peak of the Si $2s$ core level. (B,C) Spectra with background subtraction (B) before and (C) after deposition of the IPr-NHO monolayer. From the intensity ratio between the B_1 and B_2 components in (C), a coverage of 0.21±0.05 molecules per $\sqrt{3}\times\sqrt{3}$ cell is determined. (E,F) Spectra with background subtraction (B) before and (C) after deposition of the IMe-NHO monolayer. Here, a coverage of 0.32±0.05 molecules per $\sqrt{3}\times\sqrt{3}$ cell is determined.

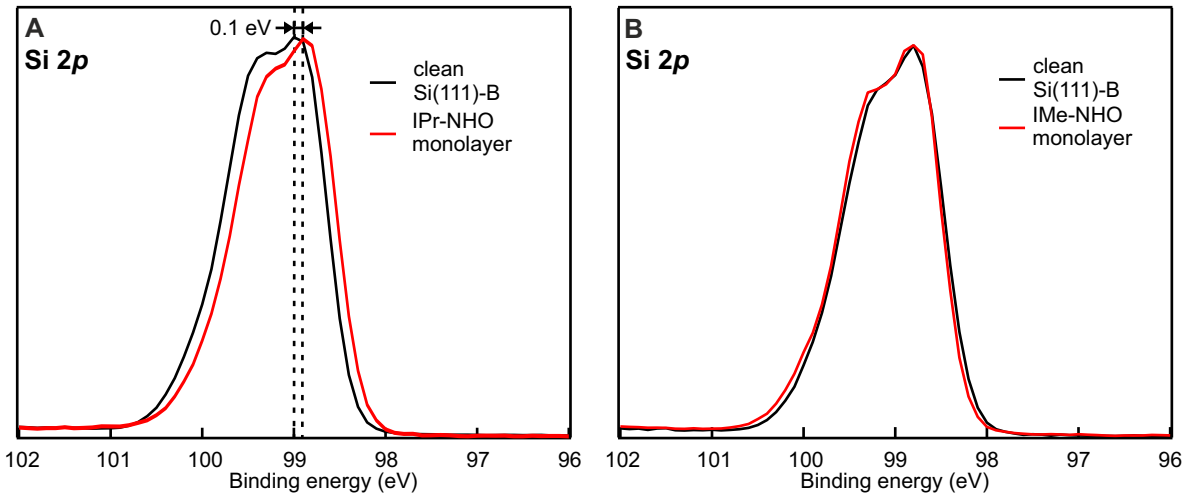

Figure S11. Si $2p$ core-level spectra for (A) the IPr-NHO monolayer and (B) the IMe-NHO monolayer. The spectra of the corresponding clean Si(111)-B samples prior to NHO deposition are shown for comparison. For better comparability, the spectra were normalized to equal height. The spectrum of the IPr-NHO monolayer appears shifted by ∼0.1 eV with respect to the clean surfaces, which is assigned to a change in band bending.

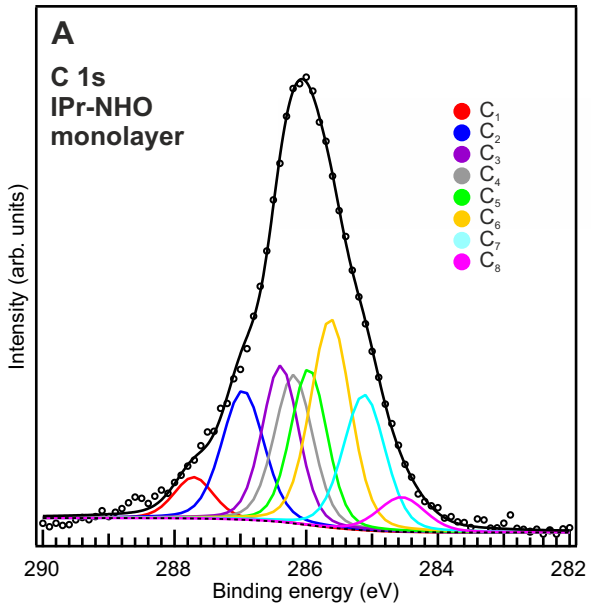

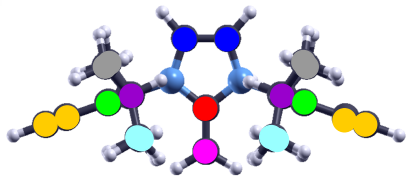

C

Component	CLS IPr-NHC theory (eV)	CLS IPr-NHC experiment (eV)	CLS IPr-NHO experiment (eV)
C_1	+1.6	+1.98	+2.08
C_2	+1.41	+1.35	+1.33
C_3	+0.95	+0.86	+0.76
C_4	+0.73	+0.65	+0.56
C_5	+0.35	+0.29	+0.33
C_6	0	0	0 (285.63)
C_7	–0.2	–0.55	-0.51
C_8	-	-	-1.08

Figure S12. (A) C 1*s* core-level spectrum of the IPr-NHO monolayer. (B) Assignment of the components to the different carbon atom sites in the molecule. Guided by the theoretical calculations performed for IPr-NHC in Ref. 3, the spectrum is decomposed in eight components. Of these components, C_1 to C_7 correspond to respective C atoms that are also present in IPr-NHC, while one component with single intensity (C_8) is added to account for the additional C_{exo} atom. The overall spectral shape is very similar to the C 1s spectrum of the IPr-NHC monolayer.[3] To examine if a similar geometry is found for the two molecules we did not perform a free fit with the least possible number of components, but tried to fit the spectrum by applying the same components and core-level shifts (CLS) as found for IPr-NHC. As demonstrated by the comparison of the CLS shown in (C), a very good agreement is obtained strongly pointing towards similar adsorption geometries for IPr-NHO and IPr-NHC. Otherwise, different CLS would be expected. Only the CLSs for C_{exo} and C_{endo} differ. Their energetic positions are again related to the ylidic structure with negative (positive) charge resulting in different screening strengths and thus lower (higher) binding energies. Note that the nomenclature of the components is slightly different from the one in Ref. 3.

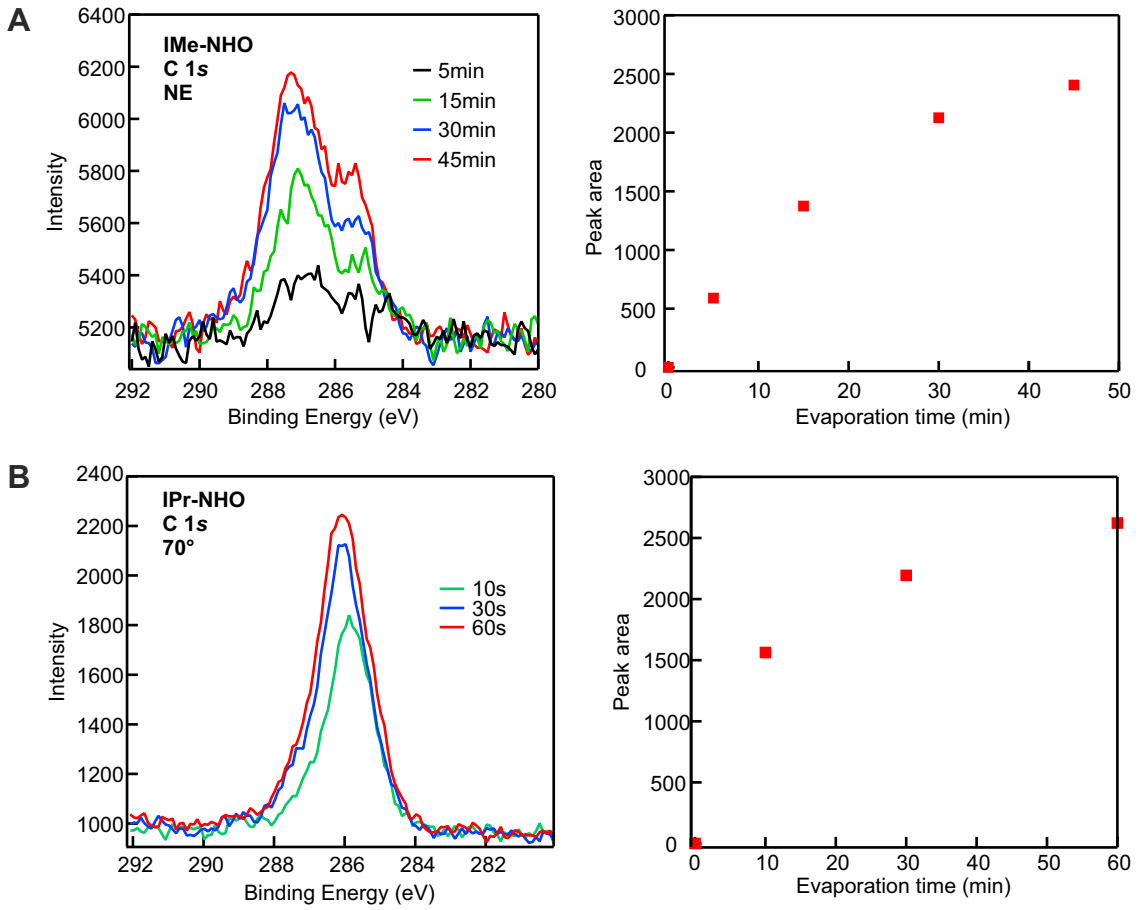

Figure S13. Coverage dependent XPS of the C 1*s* core level (left) and dependence of the area of the C 1*s* spectra on the deposition time (right) for (A) IMe-NHO and (B) IPr-NHO. The curves clearly show a saturation behavior assigned to a saturation of the stable molecular coverage at one monolayer.

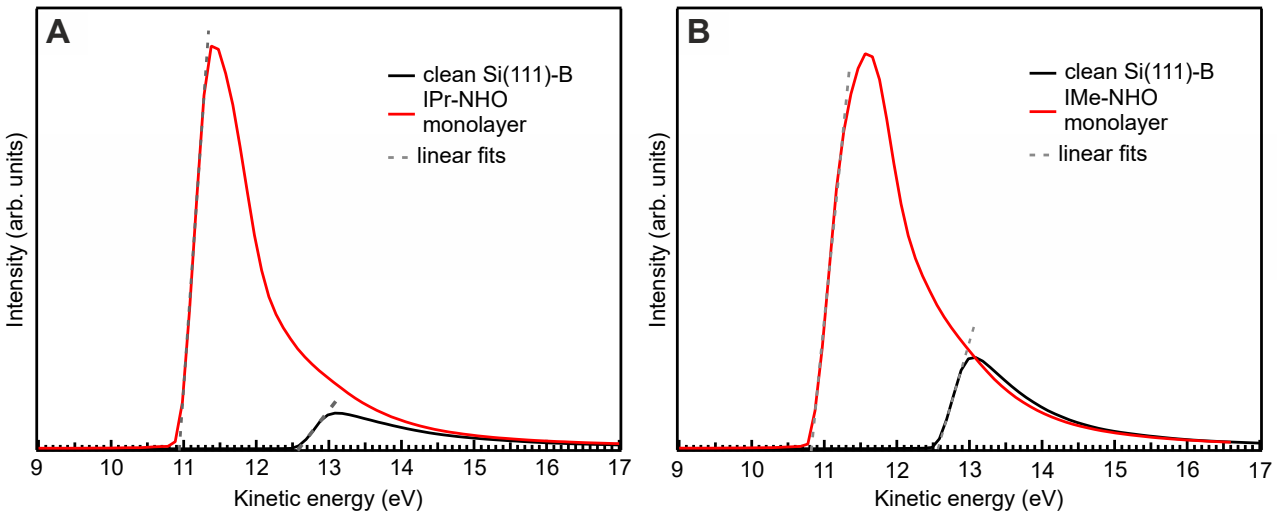

Figure S14. Secondary electron onsets measured using XPS to determine the work function reduction for (A) the IPr-NHO monolayer and (B) the IMe-NHO monolayer (red curves). The black curves show the secondary electron onsets for the corresponding clean Si(111)-B substrates prior to the NHO deposition. From the difference of the onsets determined by linear fits to the curves (dashed lines), the work function reduction is obtained.

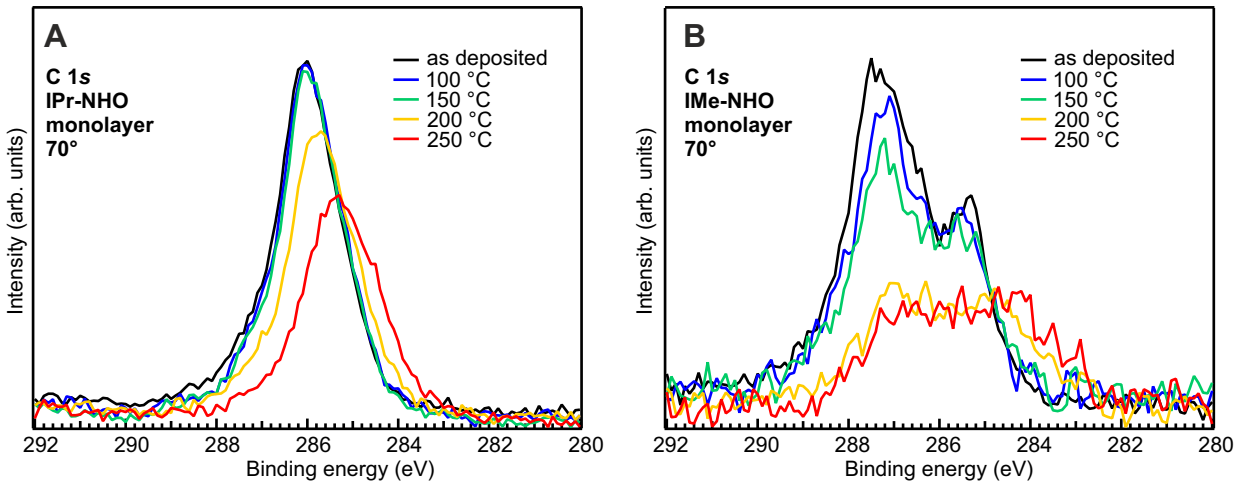

Figure S15. C 1*s* spectra for (A) the IPr-NHO and (B) the IMe-NHO monolayers measured as deposited and for different annealing steps between 100°C and 250 °C to investigate the thermal stability.

References

[1] H. Lüth, *Solid Surfaces, Interfaces and Thin Films*, Springer, Cham, 6 edition **2014**.
[2] G. Wang, A. Rühling, S. Amirjalayer, M. Knor, J. B. Ernst, C. Richter, H.-J. Gao, A. Timmer, H.-Y. Gao, N. L. Doltsinis, F. Glorius, H. Fuchs, *Nat. Chem.* **2017**, *9*, 152.
[3] M. Franz, S. Chandola, M. Koy, R. Zielinski, H. Aldahhak, M. Das, M. Freitag, U. Gerstmann, D. Liebig, A. K. Hoffmann, M. Rosin, W. G. Schmidt, C. Hogan, F. Glorius, N. Esser, M. Dähne, *Nat. Chem.* **2021**, *13*, 828–835.
[4] M. Fèvre, J. Pinaud, A. Leteneur, Y. Gnanou, J. Vignolle, D. Taton, K. Miqueu, J.-M. Sotiropoulos, *J. Am. Chem. Soc.* **2012**, *134*, 6776.
[5] M. Trujillo, S. L. Strausser, J. C. Becca, J. F. DeJesus, L. Jensen, D. M. Jenkins, J. P. Camden, *J. Phys. Chem. Lett.* **2018**, *9*, 6779.
[6] G. Kaur, R. L. Thimes, J. P. Camden, D. M. Jenkins, *Chem. Commun.* **2022**, *58*, 13188.
[7] A. J. Veinot, M. B. E. Griffiths, I. Singh, J. A. Zurakowski, P. A. Lummis, S. T. Barry, C. M. Crudden, *Mater. Adv.* **2022**, *3*, 6446.
[8] P. Giannozzi, O. Andreussi, T. Brumme, O. Bunau, M. Buongiorno Nardelli, M. Calandra, R. Car, C. Cavazzoni, D. Ceresoli, M. Cococcioni, N. Colonna, I. Carnimeo, A. Dal Corso, S. de Gironcoli, P. Delugas, R. A. DiStasio, A. Ferretti, A. Floris, G. Fratesi, G. Fugallo, R. Gebauer, U. Gerstmann, F. Giustino, T. Gorni, J. Jia, M. Kawamura, H.-Y. Ko, A. Kokalj, E. Küçükbenli, M. Lazzeri, M. Marsili, N. Marzari, F. Mauri, N. L. Nguyen, H.-V. Nguyen, A. Otero-de-la Roza, L. Paulatto, S. Poncé, D. Rocca, R. Sabatini, B. Santra, M. Schlipf, A. P. Seitsonen, A. Smogunov, I. Timrov, T. Thonhauser, P. Umari, N. Vast, X. Wu, S. Baroni, *J. Phys. Condens. Matter* **2017**, *29*, 465901.
[9] S. Grimme, J. Antony, S. Ehrlich, H. Krieg, *J. Chem. Phys.* **2010**, *132*.
[10] G. Henkelman, B. P. Uberuaga, H. Jónsson, *J. Chem. Phys.* **2000**, *113*, 9901.
[11] J. Tersoff, D. R. Hamann, *Phys. Rev. B* **1985**, *31*, 805.
[12] N. E. Singh-Miller, N. Marzari, *Phys. Rev. B* **2009**, *80*, 235407.
[13] C. Fonseca Guerra, J.-W. Handgraaf, E. J. Baerends, F. M. Bickelhaupt, *J. Comput. Chem.* **2004**, *25*, 189.
[14] A. O. de-la Roza, E. R. Johnson, V. Luaña, *Comput. Phys. Commun.* **2014**, *185*, 1007.
[15] K. Momma, F. Izumi, *J. Appl. Crystallogr.* **2011**, *44*, 1272.
[16] Y.-B. Wang, Y.-M. Wang, W.-Z. Zhang, X.-B. Lu, *J. Am. Chem. Soc.* **2013**, *135*, 11996.
[17] S. M. Ibrahim Al-Rafia, A. C. Malcolm, S. K. Liew, M. J. Ferguson, R. McDonald, E. Rivard, *Chem. Commun.* **2011**, *47*, 6987.
[18] R. L. Headrick, I. K. Robinson, E. Vlieg, L. C. Feldman, *Phys. Rev. Lett.* **1989**, *63*, 1253.
[19] P. Bedrossian, R. D. Meade, K. Mortensen, D. M. Chen, J. A. Golovchenko, D. Vanderbilt, *Phys. Rev. Lett.* **1989**, *63*, 1257.
[20] F. Bechstedt, *Principles of Surface Physics*, Springer, Berlin, Heidelberg **2003**.